Nano Research

Open Access

Research Article

Triboelectric nanogenerator based on changing the nanomorphology of polyoxometalates for gait monitoring of teenagers

Yijia Hao, Tuo Ji, Jing Zhang, and Weilin Chen ✉

Key Laboratory of Polyoxometalate and Reticular Material Chemistry of Ministry of Education, Northeast Normal University, Changchun 130024, China

Cite this article: *Nano Research*, **2025**, *18*, 94907192. https://doi.org/10.26599/NR.2025.94907192

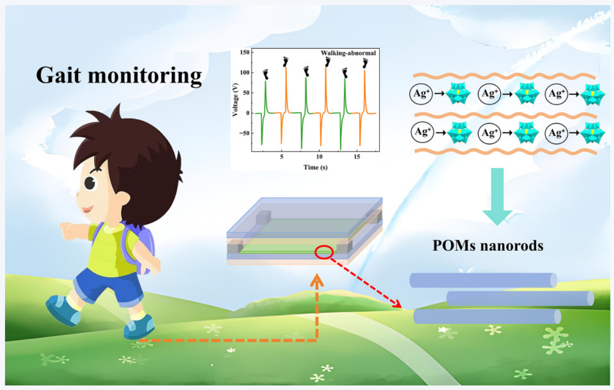

ABSTRACT: Timely monitoring abnormal gaits of teenagers is crucial for their physical health and development. Triboelectric nanogenerators (TENGs) are widely used in the wearable field. Choosing high-performance and safe triboelectric materials to monitor abnormal gaits remains challenging. Polyoxometalates (POMs) nanomaterials can effectively serve as triboelectric materials due to rich surface morphology and large specific surface area. Herein, six different sized POMs nanorods ($Ag_4SiW_{12}O_{40}\cdot nH_2O$) synthesized through self-assembly of POMs ($H_4SiW_{12}O_{40}\cdot nH_2O$) were used as triboelectric materials. The TENG composed of nanorod with a diameter of 100 nm and a length of 400–1000 nm has optimal performance with the voltage, current density and charge are 104.3 V, 1127.1 $\mu A\cdot m^{-2}$, and 15.38 nC, respectively, which are more than two times of the TENG composed of POMs ($H_4SiW_{12}O_{40}\cdot nH_2O$). The optimized TENG maintained a voltage of around 100 V throughout the 1000 s stability test. The maximum power amounts to 25.2 μW at 500 MΩ external resistance. The reasons for the improved performance of nanorods TENG compared to POMs TENG are the increase in roughness and surface potential, which was confirmed through atomic force microscopy (AFM) and kelvin probe force microscopy (KPFM) testing. Furthermore, optimized TENG was applied to the feet of different teenagers and the left and right feet of the same person to monitor abnormal gait. The changes in voltage can sensitively display the inconsistency and abnormal situations of gaits. This study confirms the potential and unique advantages of POMs nanomaterials as triboelectric materials and provides a design scheme for gait monitoring.

KEYWORDS: polyoxometalates, polyoxometalates nanomaterials, nanorods, triboelectric nanogenerator

1 Introduction

For a long time, the healthy growth of teenagers has received widespread attention from society [1, 2]. Teenagers are in a critical period of skeletal development, during which incorrect gait not only affects their appearance, but also leads to bent postures, low athletic abilities, and increases risk of sports injuries [3–5]. More seriously, these can affect the development of their bones and joints, leading to terrible problems such as flat feet, pelvic tilt, and scoliosis [6, 7]. Among these, adolescent idiopathic scoliosis (AIS) is the most common adolescent disease in recent years, affecting 2%–3% of adolescents under the age of 16 [8]. Severe scoliosis increases the risk of decreased lung capacity and limited cardiopulmonary function [9, 10]. Therefore, it is very important to choose a suitable wearable device for timely monitoring of abnormal gait in adolescents [11].

Triboelectric nanogenerators (TENG), with the advantage of effectively collecting mechanical energy from the surrounding environment, have become a research hotspot in the field of wearable electronics technology [12–14]. Wearable TENG can be worn directly on the body or integrated into clothing and accessories of the users [15, 16]. In 2024, Wang et al. prepared a TENG skin patch based on Mxene, which was first used to accelerate wound healing and tactile sensing, it has broad application prospects in biomedical fields [17]. In 2023, Yang et al. designed an intelligent clothing system using a new environmentally friendly and superhydrophobic TENG to monitor motion signals, and further applied it to sports and health

Received: September 7, 2024; **Revised:** November 7, 2024
Accepted: December 13, 2024

✉Address correspondence to chenwl@nenu.edu.cn

monitoring systems [18]. TENG can also be applied in the field of gait recognition analysis [19–21]. In 2024, Yang et al. designed a self-powered TENG gait analysis system based on electrospinning to monitor human motion [22]. Although triboelectric materials have a wide range of choices, most of the triboelectric materials used in wearable TENGs are still traditional cellulose materials and polymer materials [23–25]. Cellulose has good biocompatibility, excellent flexibility and mechanical properties, but still face performance defects such as flammability and lack of high temperature resistance [26, 27]. Polymer materials, have disadvantages such as poor washing resistance, lack of breathability, and incompatibility with clothing [28, 29]. Therefore, finding new triboelectric materials to expand the triboelectric series and improve the output performance of triboelectric materials remains challenging [30, 31]. The main method to optimize the performance of triboelectric materials is to increase roughness and current density, and the patterning and morphological changes of many materials will play corresponding roles [32–34]. In addition, selecting suitable, high-performance, and environmentally friendly triboelectric materials is a necessary condition for TENG as a wearable device [35, 36].

Polyoxometalates (POMs) nanomaterials, synthesized by constructing POMs as functional and structural units into nanostructures, has been extensively studied in the past few decades [37–41]. They possess excellent physical and chemical properties of POMs, as well as the advantages of small size, rich surface morphology, and large specific surface area that traditional materials lack [42–44]. In recent years, the development and utilization of renewable and clean energy have become a research hotspot [45–48], POMs nanomaterials have also been widely used in this field [49–55]. In 2020, our research group prepared a multifunctional energy conversion device based on POMs/ethyl cellulose composite membrane, which can generate electricity from various all-weather environmental energy sources [56]. In 2023, our research group prepared thin films of POMs nanowires and applied them to power generation in atmospheric humidity, confirming that the generator can stably and efficiently generate electricity in almost all natural environments [57]. At the same time, in 2019, our research group for the first time introduced POMs into the field of nanogenerators, providing new research ideas for the research of nanogenerators [58]. In the following years, we continued to apply POMs nanomaterials in TENG research [59, 60]. We believe that the unique advantages of POMs nanomaterials can provide convenience for triboelectric materials. Firstly, POMs nanomaterials have the advantages of large specific surface area, high roughness, and rich surface morphology, which can improve their performance as triboelectric materials [61, 62]. Secondly, compared to expensive metal triboelectric materials and complex polymer materials, the synthesis of POMs nanomaterials is simple, cost-effective, and relatively inexpensive [63, 64]. Thirdly, POMs nanomaterials are high-performance and environmentally friendly materials that playing an important role in many biochemical fields [65, 66]. These characteristics are more suitable for them as triboelectric materials to prepare wearable TENGs for monitoring the gait of adolescents.

In this study, six one-dimensional POMs nanorods $Ag_4SiW_{12}O_{40}{\cdot}nH_2O$ (named nanorods Ag-SiW_{12}-*X*, *X* = 1, 2, 3, 4, 5, and 6) were synthesized by through the self-assembly of POM $H_4SiW_{12}O_{40}{\cdot}nH_2O$ (SiW_{12}) in a linear reaction field formed by polyethylene glycol (PEG) and water. The diameter and length of these nanorods can be controlled by adjusting the concentration of PEG and selecting the type of PEG, respectively. We assembled TENG with polyethylene terephthalate (PET) as the negative triboelectric layer, SiW_{12} film and six POMs nanorods (Ag-SiW_{12}-*X*) films as positive triboelectric layers. The assembled TENGs are named sequentially as TENG-0 (positive triboelectric material is SiW_{12} film), TENG-1, TENG-2, TENG-3, (the positive triboelectric materials are Ag-SiW_{12}-1, 2, 3 with a length of 400–1000 nm, and diameters of 50, 75 and 100 nm, respectively), TENG-4, TENG-5, TENG-6 (the positive triboelectric materials are Ag-SiW_{12}-4, 5, 6, with a length of 1–2 μm, and diameters of 200, 300 and 400 nm, respectively). Performance testing has shown that TENG-3 has the optimized performance with voltage, current density, and charge are 104.3 V, 1127.1 μA·m^{-2}, and 15.38 nC, which are 2.7 times, 2.4 times, and 2.1 times that of TENG-0, respectively. The stability of TENG-3 was excellent, maintaining the voltage of around 100 V after 1000 s. The maximum output power of TENG-3 is 25.2 μW when connected to a 500 MΩ load resistor. Through atomic force microscopy (AFM) and kelvinprobe force microscopy (KPFM) testing, the reasons for the performance improvement are that the roughness and surface potential of the nanorods Ag-SiW_{12}-*X* are higher than SiW_{12}. According to the performance test results, the optimized TENG-3 was applied to both feet of the teenagers for gait monitoring. The difference in gait between the different foot of the teenagers can be sensitively displayed through the change of TENG output voltage, which has the potential risk of causing health problems such as scoliosis. Gait monitoring can prompt teenagers and their parents to pay timely attention to their gait health issues. In addition, our research explains the potential application of POMs nanomaterials in the TENG field, which is beneficial for expanding the range of materials in the triboelectric series. This work has implications for the future development of gait monitoring devices for adolescents.

2 Experimental

2.1 The reagents and materials

PEG 400 (whose relative molecular mass M_r = 400), PEG 600 (M_r = 600), silver nitrate, anhydrous ethanol and other reagents are commercially available for use. Indium tin oxide (ITO) coated PET film (ITO-PET), polyimide tape, double-sided tape, sponge, copper conductive tape and other materials are also commercially purchased. The experimental water is all deionized water. We purchased all materials and reagents used in this article from Aladdin Chemical Reagent Network.

2.2 Synthesis of SiW_{12} and Ag-SiW_{12}-*X*

SiW_{12} and six nanorods Ag-SiW_{12}-*X* were prepared according to Ref. [67]. We selected two surfactants with different relative molecular weights, PEG 400 and PEG 600. Ag-SiW_{12}-*X* were prepared by controlling the volume ratio of surfactants to water. The three nanorods prepared with a ratio of PEG 400 to water of 2.5:1.0, 2.5:1.5, and 2.5:2.0 were named as Ag-SiW_{12}-1, Ag-SiW_{12}-2, and Ag-SiW_{12}-3, respectively. The three nanorods prepared with a ratio of PEG 600 to water of 2.5:1.5, 2.5:2.0, and 2.5:2.5 were named as Ag-SiW_{12}-4, Ag-SiW_{12}-5, and Ag-SiW_{12}-6, respectively. The preparation process of nanorods is shown in Fig. 1(a).

2.3 Preparation of SiW_{12} film and Ag-SiW_{12}-*X* films

Preparation of SiW_{12} film: Different masses (0.5, 1, 1.5, 2, and 2.5

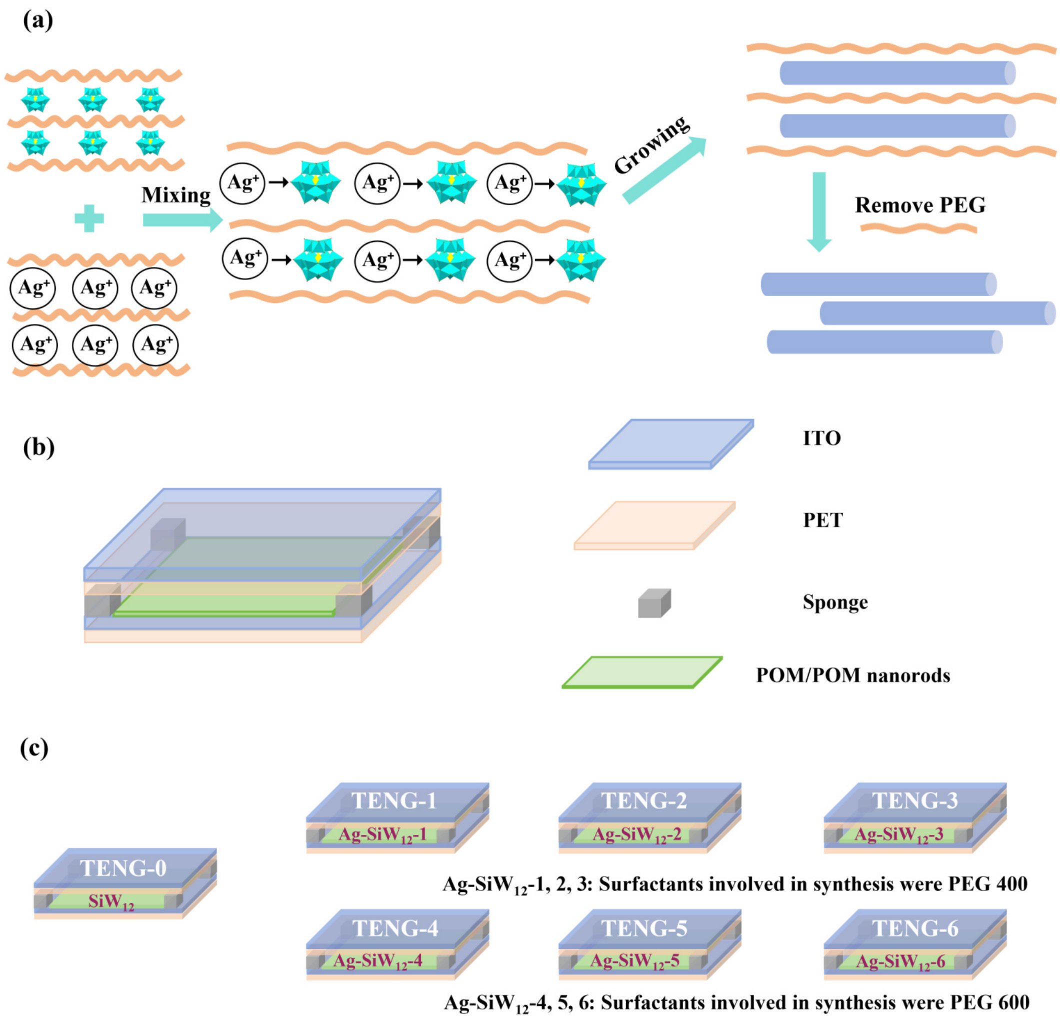

Figure 1 (a) Synthesis process of POMs nanorods. (b) TENG assembly diagram. (c) Schematic diagram of different TENGs.

mg) of SiW_{12} were dissolved in 1 mL anhydrous ethanol, and 200 mL of POMs solutions with different mass fractions were aspirated using a pipette. They were spin coated on the ITO surface of the ITO-PET material at 3000 r·min^{-1} and annealed on a 60 °C heating plate to remove solvents.

Preparation of Ag-SiW_{12}-*X* films: Six nanorods films were prepared using the same method. Taking nanorods with a ratio of 2.5:2.0 composed of PEG 400 as an example, POMs nanorods of different masses (0.5, 1, 1.5, 2, and 2.5 mg) were ultrasonically dispersed in 1 mL anhydrous ethanol. A pipette was used to extract 200 mL of suspension of Ag-SiW_{12}-*X* with different mass fractions. They were spin coated on the ITO surface of the ITO-PET material at 3000 r·min^{-1} and annealed on a 60 °C heating plate to remove solvents.

2.4 The assembly of TENGs

Taking the triboelectric nanogenerator composed of POMs nanorods as an example, we cut the ITO-PET material into 3 cm × 2 cm sizes, and attached polyimide tape on the left and right sides of each piece, making the material an effective area of 2 cm × 2 cm. We used the prepared SiW_{12} film and six POMs nanorods Ag-SiW_{12}-*X* films as the positive triboelectric layer for TENG. Take ITO-PET materials of the same size and select the PET surface as the negative triboelectric layer. Use four sponges of 0.5 cm × 0.5 cm × 0.5 cm, placed at the four corners of the sheet, so that the gap distance between the triboelectric materials is designed to be 0.5 cm. Assemble the triboelectric layers of TENG, as shown in the Fig. 1(c). Finally, use copper tape to stick onto the ITO surfaces of the two parts and connect them to the Keithley 6517B testing system. The schematic diagram of the assembled TENG device is shown in the Fig. 1(b).

SiW_{12} film and six POMs nanorods Ag-SiW_{12}-*X* films were used as triboelectric materials and assembled them with PET to form TENG, named them TENG-0, TENG-1, TENG-2, TENG-3, TENG-4, TENG-5, and TENG-6 (Fig. 1(c)).

2.5 The characterizations of materials

We characterized the composition of SiW_{12} and Ag-SiW_{12}-*X* using an Alpha Centauri FT/IR spectrophotometer (FT-IR). The morphology and element content of SiW_{12} and Ag-SiW_{12}-*X* were determined using an energy-dispersive spectrometer (EDS) and high-resolution transmission electron microscopy (HRTEM, JEOL-2100 F). Using scanning electron microscopy (SEM, Hitachi S-8010) to characterize the surface morphology and the lengths and diameters of Ag-SiW_{12}-*X*. The enhancement of nanorods-based TENG was explained by characterizing surface roughness and surface potential using AFM and KPFM, respectively.

2.6 The performance tests

Use an electrometer (Keithley 6517B) and a digital multimeter (DMM 6500) to measure three performance indicators (voltage, current density, and charge), which are the most basic physical quantities for evaluating TENG performance. Meanwhile, the stability of TENG was also tested through them. The power was measured by combining the different resistances with the external circuit.

3 Results and discussion

3.1 Characterizations of SiW_{12}, Ag-SiW_{12}-*X* and films

The SiW_{12} and six POMs nanorods Ag-SiW_{12}-*X* are characterized by FT-IR spectroscopy (Fig. S1 in the Electronic Supplementary Material (ESM)). The characteristic infrared spectrum of SiW_{12} is 1021, 970, 902, and 727 cm^{-1}, corresponded to the $\nu(Si{=}O_a)$, $\nu(W{=}O_t)$, $\nu(W{-}O_c{-}W)$, and $\nu(W{-}O_d{-}W)$ vibrational peaks of the anionic framework of SiW_{12}, respectively [68, 69]. In addition, the characteristic infrared spectra of the six POMs nanorods Ag-SiW_{12}-*X* showed that although there was a slight shift in the characteristic peaks, they all retained the structure of Keggin-type POMs, proving that the structure of SiW_{12} was not destroyed and indicating the successful preparation of Ag-SiW_{12}-*X*.

In addition, the surface morphology of SiW_{12} and the size of Ag-SiW_{12}-*X* were characterized by SEM (Fig. 2 and Figs. S2–S6 in the ESM). As shown in Fig. S2 in the ESM, Ag-SiW_{12}-*X* exhibit a nanoparticle morphology and agglomeration occurs. The size information of six POMs nanorods formed using PEG with different relative molecular weights is shown in Table S1 in the ESM. The morphology and size of Ag-SiW_{12}-3 and Ag-SiW_{12}-4 are shown in Fig. 2, while the morphology and size of other nanorods are shown in Figs. S3–S6 in the ESM. As the relative molecular weight of the surfactant increases, the length and diameter of the nanorods also increase. The principle of regulating the size of nanorods is as follows. As is well known, PEG can form a chain like structure in water. In this way, in the PEG-water liquid phase system, this chain like structure will separate the reaction space and form several linear reaction fields. When a chemical reaction occurs here, the morphology of the product is strictly limited and will grow along the opening direction of the linear reaction field. As the amount of water gradually increases, the reaction field becomes wider, and the diameter of the nanorods will increase until they are restricted by the linear reaction field and stop growing. Changing the type of PEG can achieve control over the length of nanorods [67].

In addition, we characterized the morphology of the nanorods through TEM (Figs. S7–S12 in the ESM), which also demonstrated the successful synthesis of nanorod morphology. The composition and distribution of elements in the material were determined through element mapping diagrams, as shown in Figs. S7–S12 in the ESM. Ag-SiW_{12}-*X* are composed of Si, W elements from SiW_{12} and Ag elements from $AgNO_3$, and the distribution of elements is uniform. The energy dispersive X-ray (EDX) spectrum can further confirm the composition of the nanorods, indicating the successful preparation of the nanorods.

We characterized the elements and valence states of SiW_{12} and two high-performance POMs nanorods Ag-SiW_{12}-3 and Ag-SiW_{12}-4 using X-ray photoelectron spectroscopy (XPS). Figure 3(a) shows the survey spectrum of SiW_{12}, Ag-SiW_{12}-3 and Ag-SiW_{12}-4, indicating that SiW_{12} is composed of Si, W, and O elements, while Ag-SiW_{12}-3 and Ag-SiW_{12}-4 are composed of Si, W, O, and Ag elements. The binding energies of W element W $4f_{7/2}$ and W $4f_{5/2}$ in SiW_{12} are 36.23 and 38.42 eV, respectively, corresponding to W^{6+} ions (Fig. 3(b)) [70, 71]. The binding energies of W element W $4f_{7/2}$ and W $4f_{5/2}$ in Ag-SiW_{12}-3 are located at 36.04 and 38.16 eV, respectively, corresponding to W^{6+} ions (Fig. 3(e)) [70, 71]. The binding energies of Ag $3d_{5/2}$ and Ag $3d_{3/2}$ in Ag-SiW_{12}-3 are 368.43 and 374.43 eV, respectively, indicating that Ag exists in the form of +1 valence in the sample (Fig. 3(d)) [72, 73]. The binding energies of W element W $4f_{7/2}$ and W $4f_{5/2}$ in Ag-SiW_{12}-4 are located at 35.79 and 37.94 eV, respectively, corresponding to W^{6+} ions (Fig. 3(h)) [70, 71]. The binding energies of Ag $3d_{5/2}$ and Ag $3d_{3/2}$ in Ag-SiW_{12}-4 are 368.62 and 374.78 eV, respectively, indicating that Ag exists in the form of +1 valence in the sample (Fig. 3(g)) [72, 73].

3.2 The electrical performance for TENGs

To evaluate whether improving the nano morphology of triboelectric materials would affect the output performance of TENG, we compared the performance of TENG-1 to TENG-6 assembled with Ag-SiW_{12}-*X* and TENG-0 assembled with SiW_{12} films. Based on preliminary experiments, we prepared TENGs composed of SiW_{12} and Ag-SiW_{12}-*X* with mass fraction gradients of 0.5, 1, 1.5, 2, and 2.5 $mg\cdot mL^{-1}$, and tested their electrical properties under the same experimental conditions.

The output performance of TENG-0 is as follows (Figs.

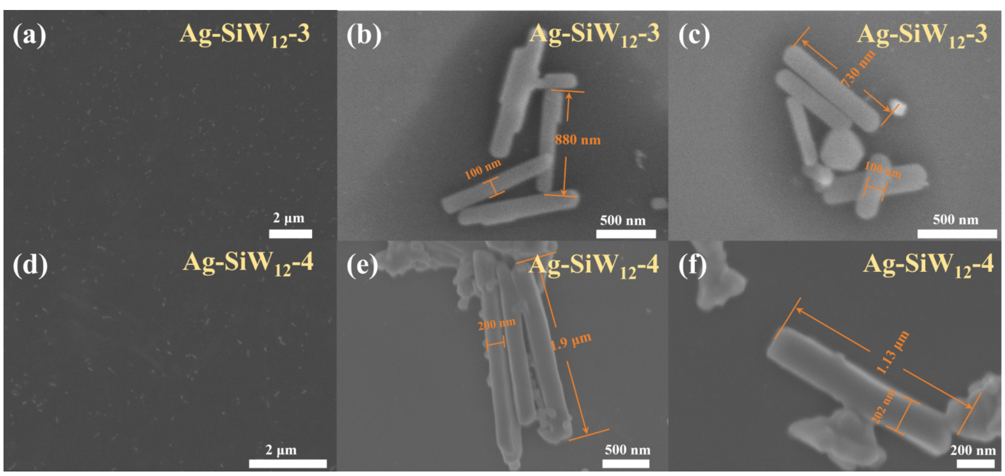

Figure 2 SEM characterization of POMs nanorods. (a)–(c) Morphology of Ag-SiW_{12}-3. (d)–(f) Morphology of Ag-SiW_{12}-4.

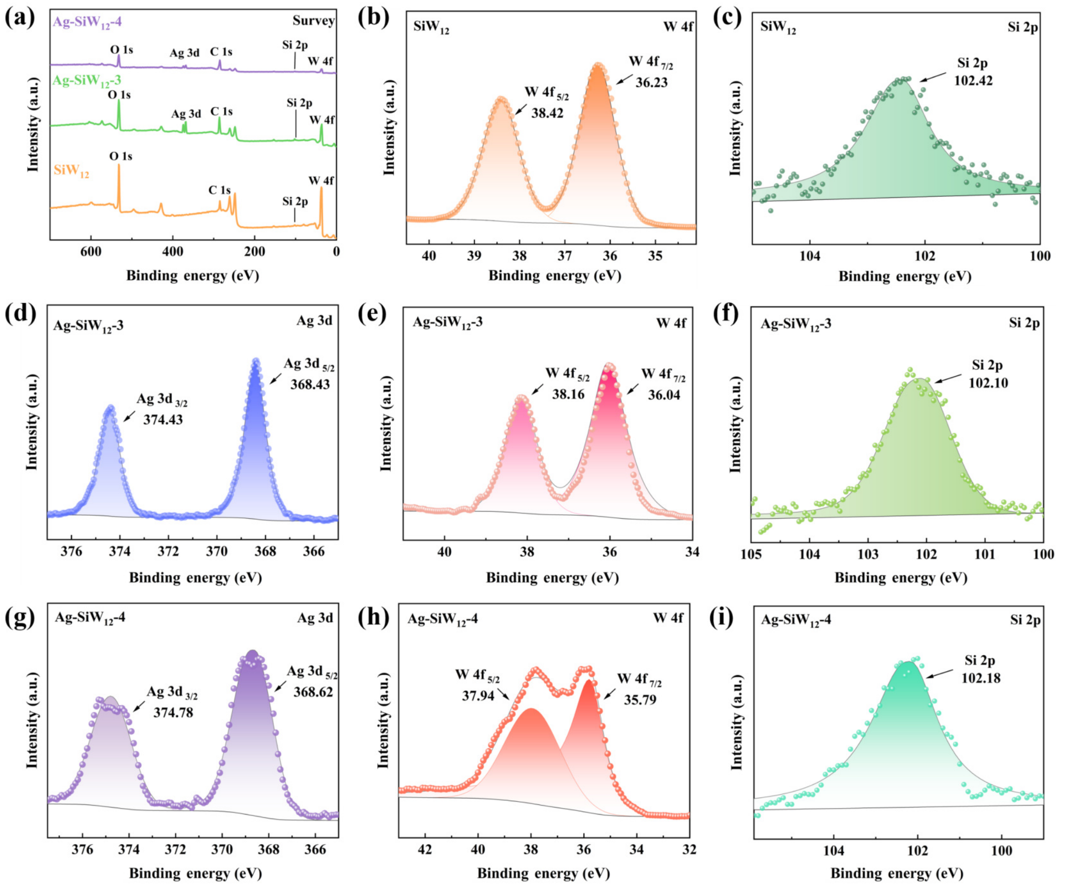

Figure 3 XPS spectra of SiW_{12}, Ag-SiW_{12}-3 and Ag-SiW_{12}-4. (a) XPS survey spectra of SiW_{12}, Ag-SiW_{12}-3 and Ag-SiW_{12}-4. (b) and (c) XPS spectra of W 4f and Si 2p for SiW_{12}. XPS spectra of (d) Ag 3d, (e) W 4f, and (f) Si 2p for Ag-SiW_{12}-3. XPS spectra of (g) Ag 3d, (h) W 4f, and (i) Si 2p for Ag-SiW_{12}-4.

4(a)–4(c)). The maximum output performance of TENG-0 occurs at a mass fraction of 2.0 mg·mL^{-1}. The instantaneous maximum voltage, current density, and transfer charge are 38.7 V, 471.7 μA·m^{-2}, and 5.99 nC, respectively. The output characteristics of the first group of Ag-SiW_{12}-1, Ag-SiW_{12}-2, and Ag-SiW_{12}-3 synthesized by PEG 400 as TENG triboelectric materials are as follows (Figs. S13 and S14 in the ESM and Figs. 4(d)–4(f)). Among them, TENG-3 has the optimal output performance, with instantaneous maximum voltage, current density, and transfer charge of 104.3 V, 1127.1 μA·m^{-2}, and 15.38 nC, respectively. The output properties of the second group of Ag-SiW_{12}-4, Ag-SiW_{12}-5, and Ag-SiW_{12}-6 synthesized by PEG-600 as TENG triboelectric materials are as follows (Figs. S15 and S16 in the ESM and Figs. 4(g)–4(i)). Among them, TENG-4 has the optimal output performance, with instantaneous maximum voltage, current density, and transfer charge of 94.0 V, 926.8 μA·m^{-2}, and 11.94 nC, respectively. According to the data, it can be seen that the output performance of TENG-0 to TENG-6 shows a trend of increasing first and then decreasing with the increase of mass fraction, which is caused by the aggregation of POMs and the stacking of nanorods [74, 75]. We can observe that the optimal performing TENGs, TENG-3 and TENG-4, have improved performance compared toTENG-0. The open circuit voltage, current density, and charge of the TENG-3 are 2.7 times, 2.4 times, and 2.6 times higher than those of TENG-0 respectively. The open circuit voltage, current density, and charge of TENG-4 are 2.4 times, 2 times, and 2 times higher than those of TENG-0, respectively.

As Figs. 5(a)–5(d) shown, comparing the optimal performance of TENG-1 to TENG-6 composed of Ag-SiW_{12}-X as triboelectric materials with TENG-0 composed of SiW_{12} as triboelectric materials, we can conclude that the three properties of TENG-1 to TENG-6 are much greater than TENG-0. In summary, by self-assembly to change the morphology of POMs, POMs nanomaterials can be synthesized, which can improve the triboelectric performance of POMs as triboelectric materials. The performance of TENG is related to the size of the triboelectric material. (1) The performance of TENG-1 to TENG-3 composed of 400–1000 nm long nanorods synthesized in a liquid environment of PEG 400 and water increases with the increase of nanorod diameter. TENG-3 performs well among them. (2) The performance of TENG-4 to TENG-6 composed of 1–2 μm long nanorods synthesized from PEG 600 and water as a liquid environment decreases with the increase of nanorod diameter. TENG-4 performs well among them. (3) In TENG composed of six nanorods from two series as triboelectric materials, TENG-3 and TENG-4 have better performance, with TENG-3 being the most optimized. We can conclude that the diameter of the nanorod will affect its performance as a triboelectric material, and the performance will first increase and then decrease with the increase of diameter.

In order to further evaluate the actual output performance of nanorods-TENG, we selected the two TENGs with the optimal performance, TENG-3 and TENG-4, for subsequent power testing. Our team connects the load to the circuit and gradually changes the load value. The research results indicates that as various loads are connected in the external circuit, the current continuously decreases

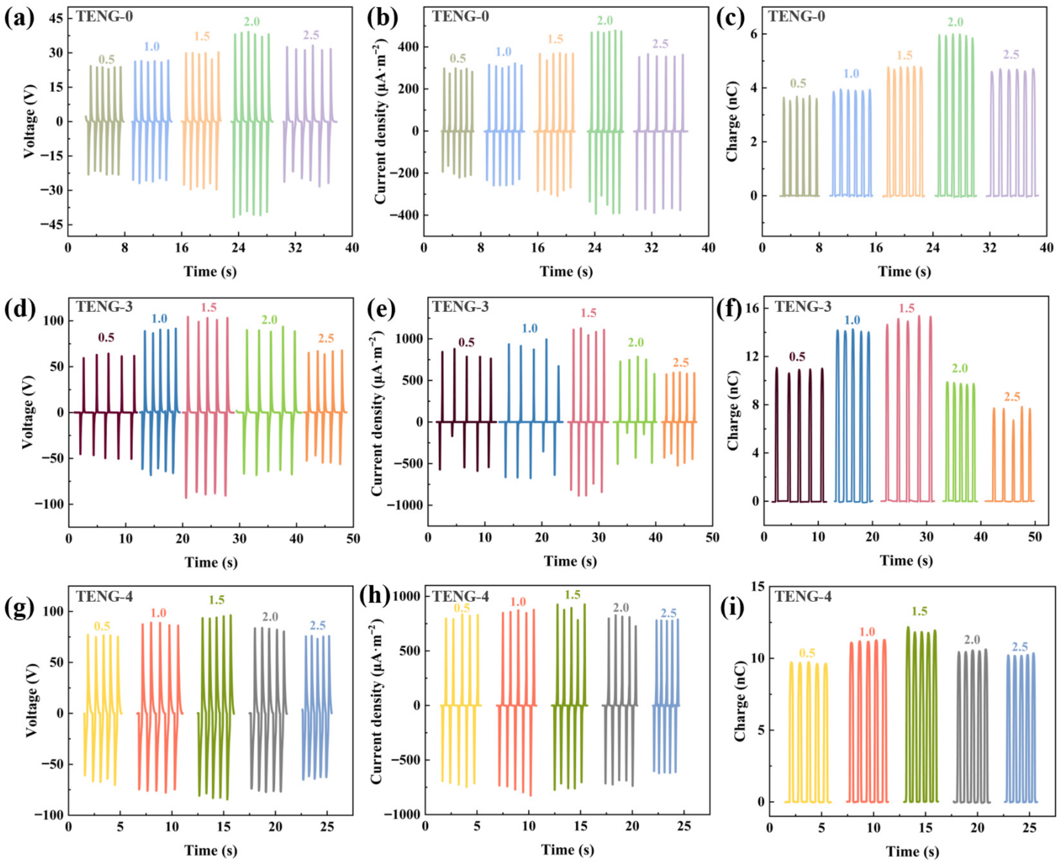

Figure 4 The output performance of TENGs. (a) The V_{OC}, (b) current density, and (c) Q_{SC} of TENG-0. (d) The V_{OC}, (e) current density, and (f) Q_{SC} of TENG-3. (g) The V_{OC}, (h) current density, and (i) Q_{SC} of TENG-4.

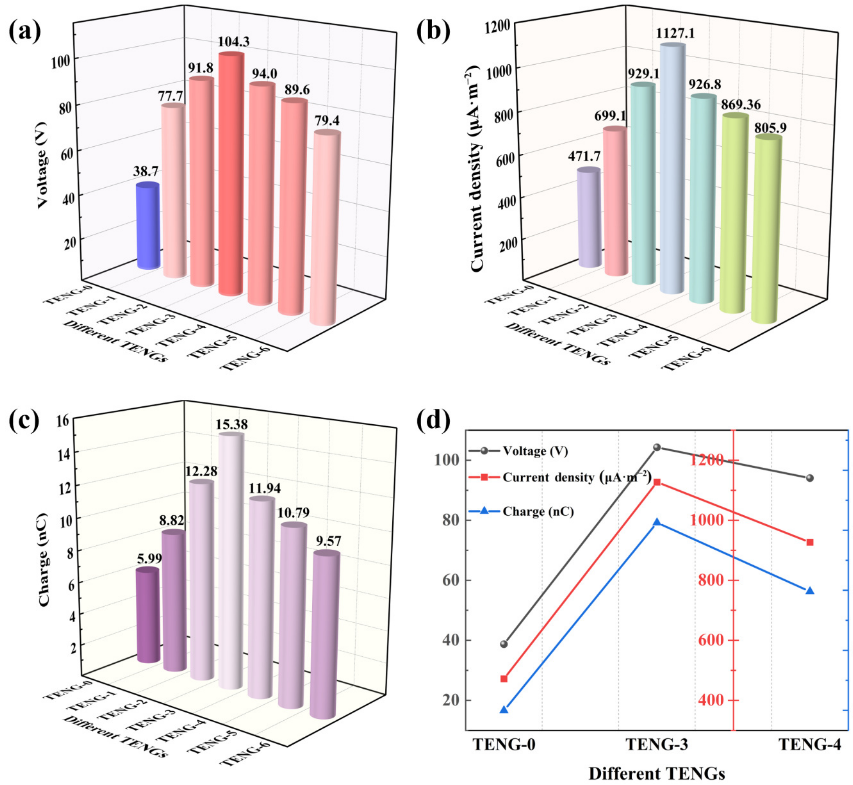

Figure 5 Comparison of TENGs performance. (a) Comparison bar chart of output voltage from TENG-0 to TENG-6. (b) Comparison bar chart of current density from TENG-0 to TENG-6. (c) Charge comparison bar chart from TENG-0 to TENG-6. (d) Line chart comparing the performance of TENG-3, TENG-4, and TENG-0.

and the voltage continuously increases, which is consistent with the regularity of TENG (Figs. 6(a)–6(d), Tables S2 and S3 in the ESM). When the load is 500 MΩ, the maximum instantaneous power of TENG-3 reached 25.2 μW (Fig. 6(a)). When the load is 500 MΩ, the maximum instantaneous power of TENG-4 reached 20.28 μW (Fig. 6(c)). The instantaneous power of TENG-3 is greater than that of TENG-4, which is consistent with other performance modes of nanorods mentioned earlier. We continued to select the TENG-3 with the best performance for stability testing, the voltage value of TENG-3 remained around 100 V even after 1000 s of operation, indicating that the device has a high level of durability (Fig. 6(e)).

3.3 The mechanism of TENG

In this study, we used PET as the negative triboelectric material, which is located in the negative electrode series and has only lower negative electrode performance than a very few materials [76]. In negative electrical materials, it has high electron attraction ability and large negative polarity. SiW_{12} and six POMs nanorods Ag-SiW_{12}-X have positive charge attraction ability and are used as positive triboelectric materials.

The mechanism of TENG-0 to TENG-6 is shown in Fig. 7. By pressing, POMs/POMs nanorods and PET come into contact and friction. Due to the difference in electronegativity, negative charges are generated on the surface of PET, positive charges are distributed on the surface of POMs/POMs nanorods. When external forces are released, the positive and negative triboelectric materials gradually move away. Due to electrostatic induction, there is a potential difference between the upper and lower electrodes of TENG, which causes electrons to flow along the external circuit from the top electrode to the bottom electrode. As the separation distance increases, the potential difference gradually increases. When the separation distance is maximum, TENG reaches electrostatic equilibrium and no current is generated. When TENG is pressed again, electrons will move in reverse from the bottom electrode to the top electrode, reaching charge balance when POMs/POMs nanorods come into maximum contact with PET. TENG achieves output performance through this iterative process [30, 77].

The reasons for the improved performance of POMs nanorods TENG are as follows. The first reason is that from a physical perspective, changing the morphology from POMs to POMs nanorods morphology will increase surface roughness, which has a promoting effect on the output performance of TENG [78–80]. The roughness of SiW_{12} film, Ag-SiW_{12}-3 film, and Ag-SiW_{12}-4 film were characterized by AFM, as shown in Figs. 8(a)–8(c). Their root mean square (RMS) values of roughness are 9.78, 33.6 and 43.3 nm, respectively. The roughness values of the three materials are: Ag-

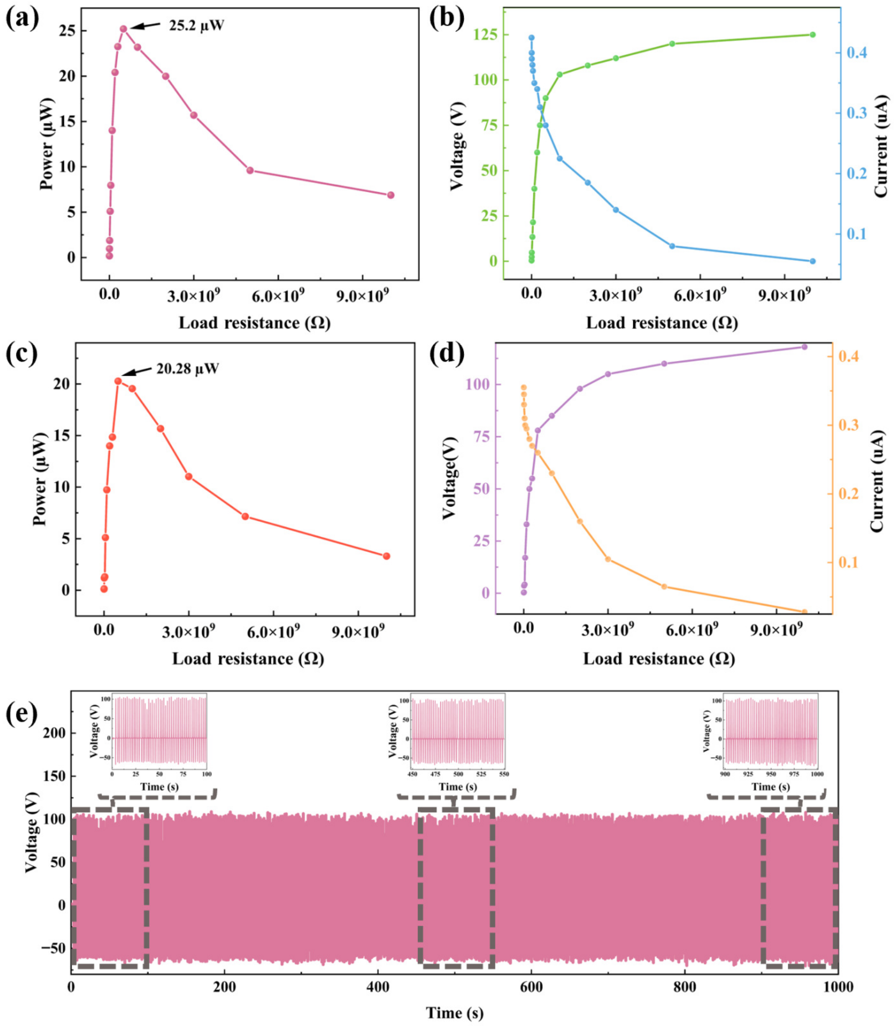

Figure 6 (a) and (b) As the load increases, the changes in current, voltage and power of TENG-3. (c) and (d) As the load increases, the changes in current, voltage and power of TENG-4. (e) Stability of TENG-3 within 1000 s operation.

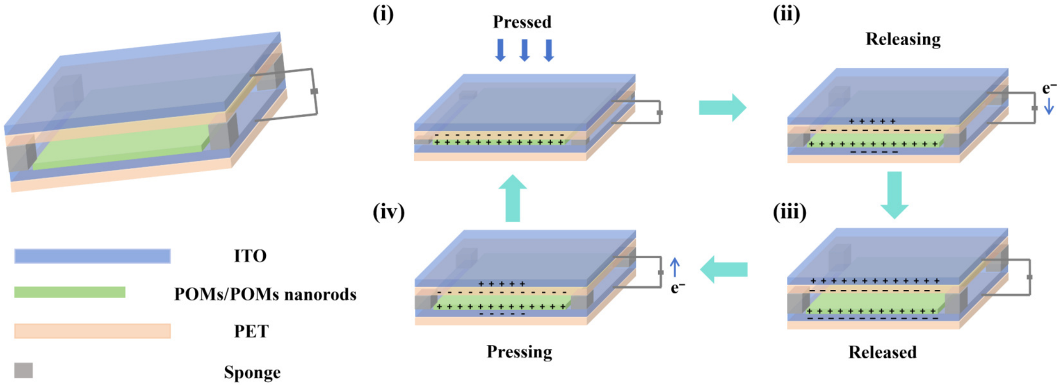

Figure 7 Working mechanism of POMs TENG and POMs nanorods TENG.

SiW_{12}-4 film is slightly higher than Ag-SiW_{12}-3 film, and the roughness of Ag-SiW_{12}-3 film and Ag-SiW_{12}-4 film is much higher than that of the SiW_{12} film. This result is basically consistent with the performance data of TENG, but the performance of TENG-4 is slightly worse than that of TENG-3, which is not very consistent with the roughness results, but the difference is tiny. So the difference in performance between the two nanorods may be caused by surface potential.

The second reason is that from a chemical perspective, the most fundamental property of friction materials is electronegativity. Therefore, KPFM was used to test the surface potential of SiW_{12}, Ag-SiW_{12}-3, and Ag-SiW_{12}-4. According to the results in Figs. 8(d)–8(f), the surface potential values of SiW_{12}, Ag-SiW_{12}-3, and Ag-SiW_{12}-4 are −0.34, −0.0481, and −0.129 V, respectively, which are consistent with their performance rules [81, 82].

The third reason is that according to XPS testing (Fig. 3), after self-assembly of SiW_{12} into Ag-SiW_{12}-X, silver ions were introduced. At the same time, we found that the binding energies of W and Si elements have changed, proving the existence of electronic interactions between Ag and POM, promoting the storage and transfer of electrons during the friction process, thereby improving the performance of nanorod-TENG.

3.4 The applications of TENG

The physical image of TENG composed of POMs nanorods captured by the camera is shown in Fig. 9(a). This demonstrates that the TENG we prepared has good transparency. As shown in Fig. 9(b), we also conducted UV visible light tests to characterize the transparency of POMs film, POMs nanorods films and TENGs. The transmittance order of the monolayer film is Ag-SiW_{12} > SiW_{12} > monolayer ITO-PET. The order of transmittance after assembly into TENG is Ag-SiW_{12} TENG > SiW_{12} TENG > double-layer ITO-PET. The improvement of morphology by POMs to POMs nanorods did not decrease the transmittance, but rather increased it. The reason why the preparation of SiW_{12} film and Ag-SiW_{12} film on ITO-PET did not reduce the transmittance but instead increased it is due to the refractive effect of the film material [83]. This phenomenon indicates that the transmittance of the TENG we tested as a wearable device is feasible. In addition, as shown in Figs. 9(c) and 9(d), the nanorod-TENG we prepared has good flexibility and can be bent freely, which fully demonstrates the promising development prospects of this TENG in the field of flexible wearable materials.

The health issues of teenagers cannot be ignored. In recent years, an increasing number of teenagers have developed health problems due to incorrect gait. Poor sitting posture and incorrect walking posture can lead to various health problems, such as scoliosis and flat feet. By analyzing the signals of adolescent foot movement, abnormal gait can be monitored and parents and adolescents can be reminded to pay attention to and correct their gait in a timely

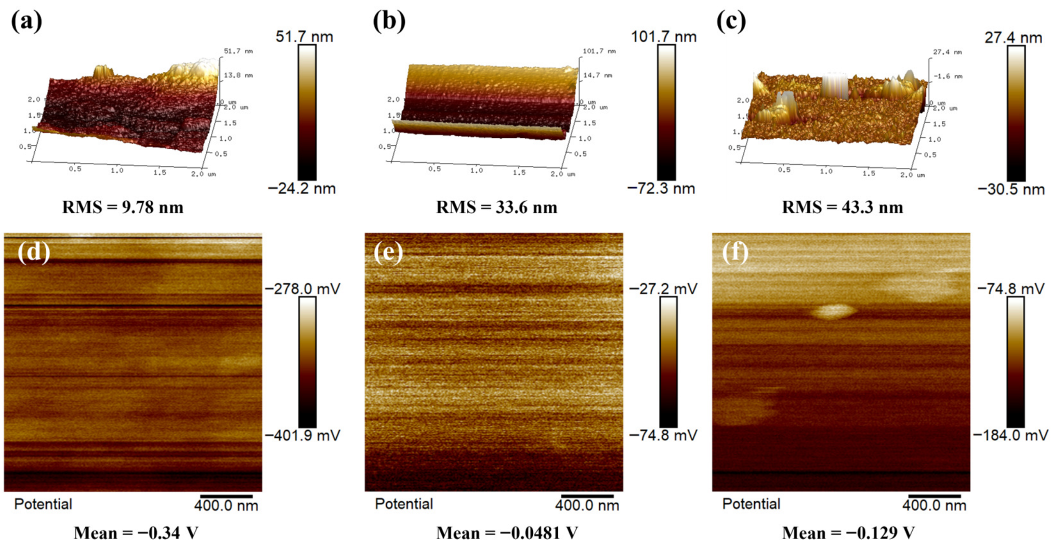

Figure 8 Surface roughness of (a) SiW_{12} film, (b) Ag-SiW_{12}-3 film, and Ag-SiW_{12}-4 film. Surface potential distribution images of (d) SiW_{12} film, (e) Ag-SiW_{12}-3 film, and (f) Ag-SiW_{12}-4 film.

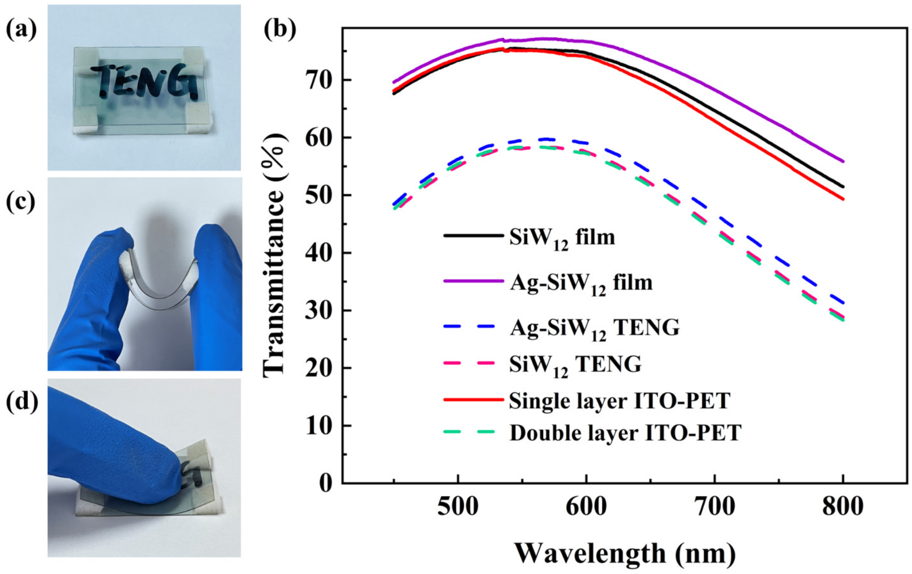

Figure 9 (a) Physical image of POMs nanorod-TENG. (b) The visible spectra of SiW_{12} film, Ag-SiW_{12} films and TENGs.

manner. In this work, we conducted application tests using TENG-3 with optimized performance.

Under normal circumstances, the force applied by the left and right feet of the human body should be similar for each gait. Therefore, our testing objective is to monitor whether the voltage values generated by the left and right feet pressing the TENG are the same during walking, running, and jumping, in order to reveal the normal and abnormal conditions of the gait. As shown in Fig. 10(a), we fixed the TENG on the ground and the experimenter sequentially used the same parts of their left and right feet to step on the device. We tested the voltage values of TENG output by 25 participants under three different gaits (walking, running, and jumping). There are two situations in each gait test. One is that some experimenters generate similar voltage values when stepping on TENG with their left and right feet in sequence, which means that the force applied by the left and right feet is basically the same (as shown in Figs. 10(b), 10(d), and 10(f)). We call it normal gait. Another situation that occurred during the test was that some experimenters generated different voltage values when stepping on their left and right feet in sequence (as shown in Figs. 10(c), 10(e), and 10(g)). This inconsistent gait may reveal abnormalities in the body, such as scoliosis, different leg lengths, flat feet, etc., which we refer to as abnormal gait. We also calculated the percentage of abnormal gait in 25 participants under three different gaits (as shown in Fig. 10(h)), as well as the specific test data for each participant (as shown in Tables S4–S6 in the ESM). Among them, 8 participants showed abnormal gait while walking, accounting for 32% of the total population; During running, 7 people showed abnormal gait, accounting for 28% of the total population; In the jumping state, 4 people showed abnormal gait, accounting for 16% of the total. Based on the above results, it can be concluded that both walking and running can sensitively detect abnormal gait. These results should draw people's attention to incorrect habits in daily life, correct abnormal gait, and prevent the formation of serious diseases.

We conducted group experiments for application's testing, and the statistical results showed POMs nanorods TENG can monitor human gait and reflect potential health issues in the human body, which provided great inspiration for wearable health monitoring devices. At the same time, the materials required for preparing TENG are inexpensive, easy to synthesize, and the resulting TENG has high transparency and good flexibility.

4 Conclusion

This study successfully used six different lengths and diameters of Ag-SiW_{12}-X nanorods which were synthesized by changing the morphology of SiW_{12} as triboelectric materials in TENG. The subsequent test results showed that the performance of nanorods-TENG was much higher than that of POMs-TENG, and the reasons for their excellent performance were explained from two aspects. In addition, we also applied nanorods-TENG to gait monitoring of teenagers, confirming its outstanding application prospects and providing new opportunities and prospects for the field. Overall, our research confirms the important role of changing the surface morphology of POMs in improving TENG performance. Currently, this application is still in the exploratory stage, and we will continue to research this gait monitoring device. We hope that this research will go out of the laboratory and provide convenience for the health of teenagers.

Electronic Supplementary Material:: Supplementary material (FT-IR spectra, SEM images, TEM images, EDS mappings, nanorods size data, TENGs performance test, power data, and application data) is available in the online version of this article at https://doi.org/10.26599/NR.2025.94907192.

Data availability

All data needed to support the conclusions in the paper are presented in the manuscript and the Electronic Supplementary Material. Additional data related to this paper may be requested from the corresponding author upon request.

Acknowledgements

This work was financially supported by the National Natural Science Foundation of China (Nos. 22271042 and 21871041), Science and Technology Research Project of the Education

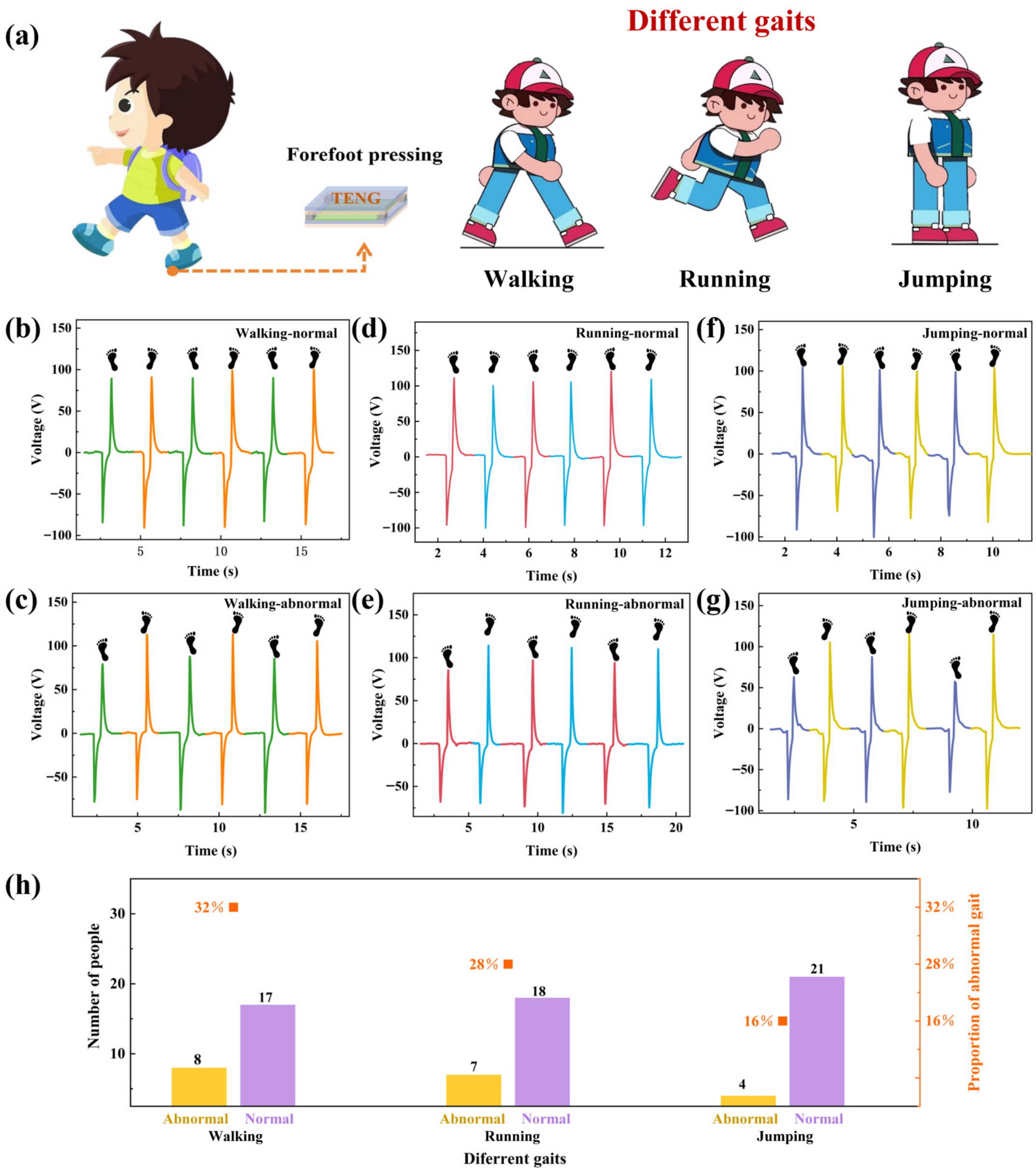

Figure 10 TENG wearable testing. (a) Test schematic diagram and three gait displays. (b) Voltage data for normal walking gait. (c) Voltage data for abnormal walking gait. (d) Voltage data for normal running gait. (e) Voltage data for abnormal running gait. (f) Voltage data for normal jumping gait. (g) Voltage data of abnormal jumping gait. (h) Statistical chart and proportion of abnormal gait during different gaits.

Department of Jilin Province (No. JJKH20211286KJ), the Natural Science Foundation of Jilin Province (No. 20180101298JC). The Fundamental Research Funds for the Central Universities (No. 2412022ZD009).

Declaration of competing interest

All the contributing authors report no conflict of interests in this work.

Author contribution statement

Y. J. H.: Writing – original draft, writing – review & editing, methodology, data curation, formal analysis, investigation, conceptualization. J. Z.: Supervision, validation. T. J.: Supervision, validation. W. L. C.: Validation, supervision, resources, funding acquisition, investigation, conceptualization. All the authors have approved the final manuscript.

Use of AI statement

None.

References

[1] Gray, N. J.; Desmond, N. A.; Ganapathee, D. S.; Beadle, S.; Bundy, D. A. Breaking down silos between health and education to improve adolescent wellbeing. *BMJ* **2022**, *379*, e067683.

[2] Chen, T. J.; Dong, B.; Dong, Y. H.; Li, J.; Ma, Y. H.; Liu, D. S.; Zhang, Y. H.; Xing, Y.; Zheng, Y.; Luo, X. M. et al. Matching actions to needs: Shifting policy responses to the changing health needs of Chinese children and adolescents. *Lancet* **2024**, *403*, 1808–1820.

[3] Sanders, J. O.; Qiu, X.; Lu, X.; Duren, D. L.; Liu, R. W.; Dang, D.;

Menendez, M. E.; Hans, S. D.; Weber, D. R.; Cooperman, D. R. The uniform pattern of growth and skeletal maturation during the human adolescent growth spurt. *Sci. Rep.* **2017**, *7*, 16705.

[4] Eltanani, S.; Olde Scheper, T. V.; Muñoz-Balbontin, M.; Aldea, A.; Cossington, J.; Lawrie, S.; Villalpando-Carrion, S.; Adame, M. J.; Felgueres, D.; Martin, C. et al. A novel criticality analysis method for assessing obesity treatment efficacy. *Appl. Sci.* **2023**, *13*, 13225.

[5] Chen, J. L.; Zhao, Y. F.; Lin, J. J.; Dai, Y. N.; Hu, B. Y.; Gao, S. A flexible insole gait monitoring technique for the internet of health things. *IEEE Sens. J.* **2021**, *21*, 26397–26405.

[6] Liu, Y. N.; Li, X. L.; Dou, X. R.; Huang, Z. G.; Wang, J.; Liao, B. G.; Zhang, X. H. Correlational analysis of three-dimensional spinopelvic parameters with standing balance and gait characteristics in adolescent idiopathic scoliosis: A preliminary research on Lenke V. *Front. Bioeng. Biotechnol.* **2022**, *10*, 1022376.

[7] Portinaro, N.; Leardini, A.; Panou, A.; Monzani, V.; Caravaggi, P. Modifying the rizzoli foot model to improve the diagnosis of pes-planus: Application to kinematics of feet in teenagers. *J. Foot Ankle Res.* **2014**, *7*, 57.

[8] US Preventive Services Task Force. Screening for adolescent idiopathic scoliosis: US preventive services task force recommendation statement. *JAMA* **2018**, *319*, 165–172.

[9] Cheng, J. C.; Castelein, R. M.; Chu, W. C.; Danielsson, A. J.; Dobbs, M. B.; Grivas, T. B.; Gurnett, C. A.; Luk, K. D.; Moreau, A.; Newton, P. O. et al. Adolescent idiopathic scoliosis. *Nat. Rev. Dis. Primers* **2015**, *1*, 15030.

[10] Wise, C. A.; Sepich, D.; Ushiki, A.; Khanshour, A. M.; Kidane, Y. H.; Makki, N.; Gurnett, C. A.; Gray, R. S.; Rios, J. J.; Ahituv, N. et al. The cartilage matrisome in adolescent idiopathic scoliosis. *Bone Res.* **2020**, *8*, 13.

[11] Li, W. C.; Lu, W. Q.; Sha, X. P.; Xing, H. L.; Lou, J. Z.; Sun, H.; Zhao, Y. L. Wearable gait recognition systems based on MEMS pressure and inertial sensors: A review. *IEEE Sens. J.* **2022**, *22*, 1092–1104.

[12] Wu, J. P.; Teng, X. R.; Liu, L.; Cui, H. Z.; Li, X. Y. Eutectogel-based self-powered wearable sensor for health monitoring in harsh environments. *Nano Res.* **2024**, *17*, 5559–5568.

[13] Wang, Z. L. From contact electrification to triboelectric nanogenerators. *Rep. Prog. Phys.* **2021**, *84*, 096502.

[14] Wang, H. B.; Han, M. D.; Song, Y.; Zhang, H. X. Design, manufacturing and applications of wearable triboelectric nanogenerators. *Nano Energy* **2021**, *81*, 105627.

[15] Zhang, R. Z.; Shen, L.; Li, J. H.; Xue, Y. Y.; Liu, H.; He, J. M.; Qu, M. N. All-fiber-based superhydrophobic wearable self-powered triboelectric nanogenerators for biomechanical and droplet energy harvesting. *ACS Appl. Nano Mater.* **2023**, *6*, 23279–23291.

[16] Feng, T. X.; Ling, D.; Li, C. Y.; Zheng, W. T.; Zhang, S. C.; Li, C.; Emel'yanov, A.; Pozdnyakov, A. S.; Lu, L. J.; Mao, Y. C. Stretchable on-skin touchless screen sensor enabled by ionic hydrogel. *Nano Res.* **2024**, *17*, 4462–4470.

[17] Mao, M. R.; Kong, J. L.; Ge, X. H.; Sun, Y. T.; Yu, H. R.; Liu, J. W.; Huang, W. M.; Wang, D. Y.; Wang, Y. Mxene-based wearable self-powered and photothermal triboelectric nanogenerator patches for wound healing acceleration and tactile sensing. *Chem. Eng. J.* **2024**, *482*, 148949.

[18] Chen, K.; Li, Y. Y.; Yang, G. G.; Hu, S. M.; Shi, Z. J.; Yang, G. Fabric-based TENG woven with bio-fabricated superhydrophobic bacterial cellulose fiber for energy harvesting and motion detection. *Adv. Funct. Mater.* **2023**, *33*, 2304809.

[19] Wei, C. H.; Cheng, R. W.; Ning, C.; Wei, X. Y.; Peng, X.; Lv, T. M.; Sheng, F. F.; Dong, K.; Wang, Z. L. A self-powered body motion sensing network integrated with multiple triboelectric fabrics for biometric gait recognition and auxiliary rehabilitation training. *Adv. Funct. Mater.* **2023**, *33*, 2303562.

[20] Zhang, D. Z.; Xu, Z. Y.; Wang, Z. H.; Cai, H. L.; Wang, J.; Li, K. S. Machine-learning-assisted wearable PVA/acrylic fluorescent layer-based triboelectric sensor for motion, gait and individual recognition. *Chem. Eng. J.* **2023**, *478*, 147075.

[21] Yeh, C.; Kao, F. C.; Wei, P. H.; Pal, A.; Kaswan, K.; Huang, Y. T.; Parashar, P.; Yeh, H. Y.; Wang, T. W.; Tiwari, N. et al. Bioinspired shark skin-based liquid metal triboelectric nanogenerator for self-powered gait analysis and long-term rehabilitation monitoring. *Nano Energy* **2022**, *104*, 107852.

[22] Zhao, L. L.; Guo, X.; Pan, Y. S.; Jia, S. C.; Liu, L. Q.; Daoud, W. A.; Poechmueller, P.; Yang, X. Y. Triboelectric gait sensing analysis system for self-powered IoT-based human motion monitoring. *InfoMat* **2024**, *6*, e12520.

[23] Lu, Z.; Jia, C. J.; Yang, X.; Zhu, Y. S.; Sun, F. X.; Zhao, T. M.; Zhang, S. W.; Mao, Y. P. A flexible TENG based on micro-structure film for speed skating techniques monitoring and biomechanical energy harvesting. *Nanomaterials* **2022**, *12*, 1576.

[24] Li, W. J.; Lu, L. Q.; Kottapalli, A. G. P.; Pei, Y. T. Bioinspired sweat-resistant wearable triboelectric nanogenerator for movement monitoring during exercise. *Nano Energy* **2022**, *95*, 107018.

[25] Miao, Y.; Zhou, M. J.; Yi, J.; Wang, Y. Y.; Tian, G. J.; Zhang, H. X.; Huang, W. L.; Wang, W. H.; Wu, R. H.; Ma, L. Y. Woven fabric triboelectric nanogenerators for human-computer interaction and physical health monitoring. *Nano Res.* **2024**, *17*, 5540–5548.

[26] Zhang, G. Y.; Liu, C.; Yang, L. J.; Kong, Y.; Fan, X.; Zhang, J.; Liu, X. Y.; Yuan, B. H. A flame-retardant and conductive fabric-based triboelectric nanogenerator: Application in fire alarm and emergency evacuation. *J. Colloid Interface Sci.* **2024**, *658*, 219–229.

[27] Wei, Z. T.; Wang, J. L.; Liu, Y. H.; Yuan, J. X.; Liu, T.; Du, G. L.; Zhu, S. Q. Y.; Nie, S. X. Sustainable triboelectric materials for smart active sensing systems. *Adv. Funct. Mater.* **2022**, *32*, 2208277.

[28] Chai, J. L.; Wang, G. L.; Zhao, J. C.; Wang, G. Z.; Wei, C.; Zhang, A. M.; Zhao, G. Q. Robust, breathable, and chemical-resistant polytetrafluoroethylene (PTFE) films achieved by novel *in-situ* fibrillation strategy for high-performance triboelectric nanogenerators. *Nano Res.* **2024**, *17*, 1942–1951.

[29] Shao, Z. C.; Chen, J. S.; Gao, K. X.; Xie, Q.; Xue, X. J.; Zhou, S. Y.; Huang, C.; Mi, L. W.; Hou, H. W. A double-helix metal-chain metal-organic framework as a high-output triboelectric nanogenerator material for self-powered anticorrosion. *Angew. Chem., Int. Ed.* **2022**, *61*, e202208994.

[30] Zou, H. Y.; Zhang, Y.; Guo, L. T.; Wang, P. H.; He, X.; Dai, G. Z.; Zheng, H. W.; Chen, C. Y.; Wang, A. C.; Xu, C. et al. Quantifying the triboelectric series. *Nat. Commun.* **2019**, *10*, 1427.

[31] Pan, X.; Zhuang, Y. X.; He, W.; Lin, C. J.; Mei, L. F.; Chen, C. J.; Xue, H.; Sun, Z. G.; Wang, C. F.; Peng, D. F. et al. Quantifying the interfacial triboelectricity in inorganic-organic composite mechanoluminescent materials. *Nat. Commun.* **2024**, *15*, 2673.

[32] Liu, X. R.; Zhao, Z. H.; Gao, Y. K.; Nan, Y.; Hu, Y. X.; Guo, Z. T.; Qiao, W. Y.; Wang, J.; Zhou, L. L.; Wang, Z. L. et al. Triboelectric nanogenerators exhibiting ultrahigh charge density and energy density. *Energy Environ. Sci.* **2024**, *17*, 3819–3831.

[33] Wang, H. M.; Xu, L.; Bai, Y.; Wang, Z. L. Pumping up the charge density of a triboelectric nanogenerator by charge-shuttling. *Nat. Commun.* **2020**, *11*, 4203.

[34] Yun, S. Y.; Kim, M. H.; Yang, G. G.; Choi, H. J.; Kim, D. W.; Choi, Y. K.; Kim, S. O. A triboelectric nanogenerator with synergistic complementary nanopatterns fabricated by block copolymer self-assembly. *J. Mater. Chem. A* **2024**, *12*, 11302–11309.

[35] Liu, L. Y.; Wu, M. J.; Zhao, W. T.; Tao, J.; Zhou, X. R.; Xiong, J. Q. Progress of triboelectric nanogenerators with environmental adaptivity. *Adv. Funct. Mater.* **2024**, *34*, 2308353.

[36] Wang, Z. K.; Hao, C. C.; Cai, M. Z.; Cui, J.; Zheng, Y. Q.; Xue, C. Y. A highoutput PDMS-MXene/gelatin triboelectric nanogenerator with the petal surface-microstructure. *Nano Res.* **2024**, *17*, 4151–4162.

[37] Ma, P. T.; Hu, F.; Wang, J. P.; Niu, J. Y. Carboxylate covalently modified polyoxometalates: From synthesis, structural diversity to applications. *Coord. Chem. Rev.* **2019**, *378*, 281–309.

[38] Gu, Y.; Wu, A. P.; Jiao, Y. Q.; Zheng, H. R.; Wang, X. Q.; Xie, Y.; Wang, L.; Tian, C. G.; Fu, H. G. Two-dimensional porous molybdenum phosphide/nitride heterojunction nanosheets for pH-universal hydrogen evolution reaction. *Angew. Chem., Int. Ed.* **2021**, *60*, 6673–6681.

[39] Song, Y. F.; Tsunashima, R. Recent advances on polyoxometalate-based molecular and composite materials. *Chem. Soc. Rev.* **2012**, *41*, 7384–7402.

[40] Wang, G. X.; Chen, X. F.; Li, B.; Wu, L. X. Near-infrared photothermal conversion of polyoxometalate-modified gold nanorods for plasmon-enhanced catalysis. *Inorg. Chem. Front.* **2023**, *10*, 1852–1862.

[41] Feng, Y. Q.; Fu, F. Y.; Zeng, L. L.; Zhao, M. Y.; Xin, X.; Liang, J. K.; Zhou, M.; Fang, X. K.; Lv, H. J.; Yang, G. Y. Atomically precise silver clusters stabilized by lacunary polyoxometalates with photocatalytic CO_2 reduction activity. *Angew. Chem., Int. Ed.* **2024**, *63*, e202317341.

[42] Cameron, J. M.; Guillemot, G.; Galambos, T.; Amin, S. S.; Hampson, E.; Mall Haidaraly, K.; Newton, G. N.; Izzet, G. Supramolecular assemblies of organo-functionalised hybrid polyoxometalates: From functional building blocks to hierarchical nanomaterials. *Chem. Soc. Rev.* **2022**, *51*, 293–328.

[43] Lu, J. K.; He, P. P.; Niu, J. Y.; Wang, J. P. Polyoxometalate-supported metal carbonyl derivatives: From synthetic strategies to structural diversity and applications. *Inorg. Chem. Front.* **2019**, *6*, 3041–3056.

[44] Yang, M. Z.; Li, H. Y.; Wang, J.; Shi, W. X.; Zhang, Q. H.; Xing, H. Z.; Ren, W. B.; Sun, B. Z.; Guo, M. F.; Xu, E. X. et al. Roll-to-roll fabricated polymer composites filled with subnanosheets exhibiting high energy density and cyclic stability at 200 °C. *Nat. Energy* **2024**, *9*, 143–153.

[45] Liao, F.; Yin, K.; Ji, Y. J.; Zhu, W. X.; Fan, Z. L.; Li, Y. Y.; Zhong, J.; Shao, M. W.; Kang, Z. H.; Shao, Q. Iridium oxide nanoribbons with metastable monoclinic phase for highly efficient electrocatalytic oxygen evolution. *Nat. Commun.* **2023**, *14*, 1248.

[46] Fan, Z. L.; Liao, F.; Shi, H. X.; Liu, Y.; Shao, M. W.; Kang, Z. H. Highly efficient water splitting over a RuO_2/F-doped graphene electrocatalyst with ultra-low ruthenium content. *Inorg. Chem. Front.* **2020**, *7*, 2188–2194.

[47] Zhu, C. C.; Xu, L.; Liu, Y. Z.; Liu, J.; Wang, J.; Sun, H. J.; Lan, Y. Q.; Wang, C. Polyoxometalate-based plasmonic electron sponge membrane for nanofluidic osmotic energy conversion. *Nat. Commun.* **2024**, *15*, 4213.

[48] Lu, M.; Zhang, M.; Liu, J.; Yu, T. Y.; Chang, J. N.; Shang, L. J.; Li, S. L.; Lan, Y. Q. Confining and highly dispersing single polyoxometalate clusters in covalent organic frameworks by covalent linkages for CO_2 photoreduction. *J. Am. Chem. Soc.* **2022**, *144*, 1861–1871.

[49] Yuan, G. B.; Ge, H. Y.; Shi, W. X.; Liu, J. L.; Zhang, Y.; Wang, X. Hybrid sub-1 nm nanosheets of co-assembled $MnZnCuO_x$ and polyoxometalate clusters as anodes for Li-ion batteries. *Angew. Chem., Int. Ed.* **2023**, *62*, e202309934.

[50] Jiao, Y. Q.; Yan, H. J.; Wang, R. H.; Wang, X. W.; Zhang, X. M.; Wu, A. P.; Tian, C. G.; Jiang, B. J.; Fu, H. G. Porous plate-like MoP assembly as an efficient pH-universal hydrogen evolution electrocatalyst. *ACS Appl. Mater. Interfaces* **2020**, *12*, 49596–49606.

[51] Liu, Y.; Yue, C. L.; Sun, F. Y.; Bao, W. J.; Chen, L. L.; Zeb, Z.; Wang, C. Z.; Ma, S. Y.; Zhang, C.; Sun, D. F. et al. Superhydrophilic molybdenum phosphide quantum dots on porous carbon matrix for boosting hydrogen evolution reaction. *Chem. Eng. J.* **2023**, *454*, 140105.

[52] Ni, L. B.; Gu, J.; Jiang, X. Y.; Xu, H. J.; Wu, Z.; Wu, Y. C.; Liu, Y.; Xie, J.; Wei, Y. G.; Diao, G. W. Polyoxometalate-cyclodextrin-based cluster-organic supramolecular framework for polysulfide conversion and guest-host recognition in lithium-sulfur batteries. *Angew. Chem., Int. Ed.* **2023**, *62*, e202306528.

[53] Bian, Y. M.; Wang, R. Z.; Xu, X. X.; Chen, J.; Wang, Q. A wheel-like polyoxometalate for haloperoxidase-inspired antibiofouling with H_2O_2 *in situ* provided by electrocatalysis. *Inorg. Chem. Front.* **2024**, *11*, 3047–3055.

[54] Zheng, Y.; Xu, X. X.; Chen, J.; Wang, Q. Surface O^{2-} regulation on POM electrocatalyst to achieve accurate 2e/4e-ORR control for H_2O_2 production and Zn-air battery assemble. *Appl. Catal. B: Environ.* **2021**, *285*, 119788.

[55] Zuo, Y. K.; Li, Y. R.; Sun, Y. Q.; Li, X. X.; Sun, C.; Zheng, S. T. Efficient catalysis of Knoevenagel condensation by 1D copper-containing heteropolyoxoniobate at room temperature. *Inorg. Chem. Front.* **2024**, *11*, 1993–1997.

[56] Wang, T.; Ji, T.; Chen, W. L.; Li, X. H.; Guan, W.; Geng, Y.; Wang, X. L.; Li, Y. G.; Kang, Z. H. Polyoxometalate film simultaneously converts multiple low-value all-weather environmental energy to electricity. *Nano Energy* **2020**, *68*, 104349.

[57] Ji, T.; Chen, W. L.; Kang, Z. H.; Zhang, L. M. Polyoxometalates for continuous power generation by atmospheric humidity. *Nano Res.* **2024**, *17*, 1875–1885.

[58] He, P.; Chen, W. L.; Li, J. P.; Zhang, H.; Li, Y. W.; Wang, E. B. Keggin and Dawson polyoxometalates as electrodes for flexible and transparent piezoelectric nanogenerators to efficiently utilize mechanical energy in the environment. *Sci. Bull.* **2020**, *65*, 35–44.

[59] Su, Y.; Liu, X. D.; Wang, H. Y.; Hao, Y. J.; Guan, L. Y.; Chen, W. L. Polyoxometalate-modified g-C_3N_4 composites with high work function for triboelectric nanogenerators. *Inorg. Chem.* **2024**, *63*, 1328–1336.

[60] Su, Y.; Ma, C. H.; Chen, W. L.; Xu, X. Y.; Tang, Q. X. Flexible and transparent triboelectric nanogenerators based on polyoxometalate-modified polydimethylsiloxane composite films for harvesting biomechanical energy. *ACS Appl. Nano Mater.* **2022**, *5*, 15369–15377.

[61] Singal, S.; Yadav, A.; Sharma, K.; Sharma, M.; Sharma, R. K. An electrochemical impedance aptasensor based on selenomolybdate nanodot/antimonene hybrid for platelet-derived growth factor-BB. *J. Mater. Chem. B* **2023**, *11*, 1958–1970.

[62] Liu, Q. D.; Wang, X. Fabricating sub-nanometer materials through cluster assembly. *Chem. Sci.* **2022**, *13*, 12280–12289.

[63] Jiang, L. J.; Li, J. F.; Xia, D. D.; Gao, M.; Li, W. Z.; Fu, D. Y.; Zhao, S. C.; Li, G. M. Lanthanide polyoxometalate based water-jet film with reversible luminescent switching for rewritable security printing. *ACS Appl. Mater. Interfaces* **2021**, *13*, 49462–49471.

[64] Chen, L.; Chen, W. L.; Wang, X. L.; Li, Y. G.; Su, Z. M.; Wang, E. B. Polyoxometalates in dye-sensitized solar cells. *Chem. Soc. Rev.* **2019**, *48*, 260–284.

[65] Song, N. Z.; Lu, M. Y.; Liu, J. C.; Lin, M.; Shangguan, P.; Wang, J. F.; Shi, B. Y.; Zhao, J. W. A giant heterometallic polyoxometalate nanocluster for enhanced brain-targeted glioma therapy. *Angew. Chem., Int. Ed.* **2024**, *63*, e202319700.

[66] Zhao, H. S.; Zhao, C. Q.; Liu, Z. W.; Yi, J. D.; Liu, X. M.; Ren, J. S.; Qu, X. G. A polyoxometalate-based pathologically activated assay for efficient bioorthogonal catalytic selective therapy. *Angew. Chem., Int. Ed.* **2023**, *62*, e202303989.

[67] Kang, Z. H.; Wang, E. B.; Jiang, M.; Lian, S. Y.; Li, Y. G.; Hu, C. W. Convenient controllable synthesis of inorganic 1D nanocrystals and 3D high-ordered microtubes. *Eur. J. Inorg. Chem.* **2003**, *2003*, 370–376.

[68] Cuentas-Gallegos, A. K.; Zamudio-Flores, A.; Casas-Cabanas, M. Dispersion of SiW_{12} nanoparticles on highly oxidized multiwalled carbon nanotubes and their electrocatalytic behavior. *J. Nano Res.* **2011**, *14*, 11–18.

[69] Xiao, C. L.; Zhang, L.; Wang, K. F.; Wang, H. P.; Zhou, Y. Y.; Wang, W. Z. A new approach to enhance photocatalytic nitrogen fixation performance via phosphate-bridge: A case study of SiW_{12}/K-C_3N_4. *Appl. Catal. B: Environ.* **2018**, *239*, 260–267.

[70] Chen, L.; Chen, W. L.; Tan, H. Q.; Li, J. S.; Sang, X. J.; Wang, E. B.

The improved efficiency of quantum-dot-sensitized solar cells with a wide spectrum and pure inorganic donor–acceptor type polyoxometalate as a collaborative cosensitizer. *J. Mater. Chem. A* **2016**, *4*, 4125–4133.

[71] Zhang, J.; Xiao, F. P.; Hao, J.; Wei, Y. G. The chemistry of organoimido derivatives of polyoxometalates. *Dalton Trans.* **2012**, *41*, 3599–3615.

[72] Jiang, B. J.; Tian, C. G.; Song, G.; Chang, W.; Wang, G. F.; Wu, Q.; Fu, H. G. A novel Ag/graphene composite: Facile fabrication and enhanced antibacterial properties. *J. Mater. Sci.* **2013**, *48*, 1980–1985.

[73] Sui, C.; Wang, Z. Y.; Wang, C.; Zhou, G. D.; Cheng, T. X. Fabrication and photocatalytic properties of water-stable Ag/PW_{12}/PVA nanocomposites. *Chem. Res. Chin. Univ.* **2016**, *32*, 854–861.

[74] Sartorel, A.; Carraro, M.; Bagno, A.; Scorrano, G.; Bonchio, M. Asymmetric tetraprotonation of γ-$[(SiO_4)W_{10}O_{32}]^{8-}$ triggers a catalytic epoxidation reaction: Perspectives in the assignment of the active catalyst. *Angew. Chem., Int. Ed.* **2007**, *46*, 3255–3258.

[75] Xu, X. Y.; Xie, M. Y.; Xu, K. C.; Zhao, Y. g-C_3N_4@PMo_{12} composite material double adjustment improves the performance of perovskite-based photovoltaic devices. *Sol. Energy* **2020**, *209*, 363–370.

[76] Fan, F. R.; Lin, L.; Zhu, G.; Wu, W. Z.; Zhang, R.; Wang, Z. L. Transparent triboelectric nanogenerators and self-powered pressure sensors based on micropatterned plastic films. *Nano Lett.* **2012**, *12*, 3109–3114.

[77] Zhu, G.; Pan, C. F.; Guo, W. X.; Chen, C. Y.; Zhou, Y. S.; Yu, R. M.; Wang, Z. L. Triboelectric-generator-driven pulse electrodeposition for micropatterning. *Nano Lett.* **2012**, *12*, 4960–4965.

[78] Wen, J.; He, H. L.; Niu, C. P.; Rong, M. Z.; Huang, Y. Q.; Wu, Y. An improved equivalent capacitance model of the triboelectric nanogenerator incorporating its surface roughness. *Nano Energy* **2022**, *96*, 107070.

[79] Xu, Y.; Min, G. B.; Gadegaard, N.; Dahiya, R.; Mulvihill, D. M. A unified contact force-dependent model for triboelectric nanogenerators accounting for surface roughness. *Nano Energy* **2020**, *76*, 105067.

[80] Zhou, Z. K.; Qin, H. F.; Cui, P.; Wang, J. J.; Zhang, J. J.; Ge, Y.; Liu, H. M.; Feng, C.; Meng, Y.; Huang, Z. Y. et al. Enhancing the output of liquid-solid triboelectric nanogenerators through surface roughness optimization. *ACS Appl. Mater. Interfaces* **2024**, *16*, 4763–4771.

[81] Liu, Y. K.; Liu, W. L.; Wang, Z.; He, W. C.; Tang, Q.; Xi, Y.; Wang, X.; Guo, H. Y.; Hu, C. G. Quantifying contact status and the air-breakdown model of charge-excitation triboelectric nanogenerators to maximize charge density. *Nat. Commun.* **2020**, *11*, 1599.

[82] Zhang, Y. Z.; Gao, X. Y.; Zhang, Y. C.; Gui, J. Z.; Sun, C. L.; Zheng, H. W.; Guo, S. S. High-efficiency self-charging power systems based on performance-enhanced hybrid nanogenerators and asymmetric supercapacitors for outdoor search and rescue. *Nano Energy* **2022**, *92*, 106788.

[83] Li, G. Z.; Wang, G. G.; Ye, D. M.; Zhang, X. W.; Lin, Z. Q.; Zhou, H. L.; Li, F.; Wang, B. L.; Han, J. C. High-performance transparent and flexible triboelectric nanogenerators based on PDMS-PTFE composite films. *Adv. Electron. Mater.* **2019**, *5*, 1800846.